Inelastic neutron scattering by quasi-crystals: A model for icosahedral Al-Mn; for Al-Mn-Pd comparison with the experimental results

1994 J. Phys.: Condens. Matter 6 659

(http://iopscience.iop.org/0953-8984/6/3/007)

J. Phys.: Condens. Matter 6 (1994) 659–678. Printed in the UK

Inelastic neutron scattering by quasi-crystals: a model for icosahedral Al–Mn; for Al–Mn–Pd comparison with the experimental results

G Poussigue†, C Benoit†, M de Boissieu‡ and R Currat§

† Groupe de Dynamique des Phases Condensées, Unité de Recherche associée au CNRS 233, Université Montpellier II, place E Bataillon, 34095 Montpellier Cédex 5, France

‡ Laboratoire de Thermodynamique et Physico-chimie Métallurgiques, Ecole Nationale Supérieure d'Electrochimie et d'Electrométallurgie de Grenoble, BP 75, 38402 St Martin d'Hères Cédex, France

§ Institut Laue–Langevin, BP 156, 38042 Grenoble Cédex 9, France

Received 18 June 1993, in final form 13 September 1993

Abstract. Using the spectral moments method, we have studied the inelastic neutron scattering by phonons in an Al–Mn quasi-crystal. The structural model is derived from the work of Duneau and Oguey. For the dynamical model we assume an effective potential with force constants depending upon equilibrium distances. Calculations are performed with the first seven rational approximants of the quasi-periodic structure. Pseudo-acoustic dispersion curves associated with intense Bragg peaks are reported. Broadening of inelastic neutron scattering peaks with increasing phonon frequency is found in high-order approximants. We compare our results with experimental spectra obtained on an Al–Mn–Pd quasi-crystal where such a behaviour has been observed. The relation of the peak broadening to the critical character of the modes is discussed.

1. Introduction

Many models have been investigated in the past few years to study the electronic and vibrational properties of quasi-crystalline systems. Most of them concern the properties of 1D or 2D systems. Only very few studies have concerned the properties of 3D systems (Janssen 1988, Hafner and Krajči' 1993, Los 1993, Los *et al* 1993). In fact, for 3D systems, there is no exact solution: calculations can be performed only for limited clusters or for rational approximants.

In this paper we present a theoretical study of the vibrational properties of the quasi-crystal Al–Mn. Although very few experimental results are available for this compound, it was interesting to develop a model because it is the simplest system which exhibits quasi-crystalline properties. It is a realistic 3D model describing the icosahedral Al–Mn (i-(Al–Mn)) phase. All the dynamical properties reported in experimental studies of various quasi-crystals can be easily derived from this simple binary model and especially the inelastic neutron scattering.

Moreover it is a good tool for reproducing the inelastic neutron scattering by icosahedral Al–Mn–Pd (i-(Al–Mn–Pd)) for the low scattering energies. The dynamical properties of the i-(Al–Mn–Pd) phase have been recently studied (de Boissieu *et al* 1993a, b). This quasi-crystal, unlike the Al–Mn phase, does not have a primitive Bravais lattice but a FCC lattice. However, this FCC structure is generated by a chemical ordering over a simple-cubic lattice.

0953-8984/94/030659+20$07.50

The basic clusters involved are similar to those in the i-(Al–Mn) phase and consist of the Mackay icosahedra. It is thus reasonable to think that dynamical properties should be similar in both phases. The differences due to the Pd atoms can be seen in only the optical part of the spectra.

The model used to describe the structure of the i-(Al–Mn) alloy is developed in section 2. In section 3 we present the dynamical model used to describe the interatomic interactions. The computational technique needed for the calculation of the scattering cross section is developed in section 4. The results of the computation are presented in section 5 where they are compared with experimental results.

In the last section we discuss the origin of the broadening of the neutron peaks.

2. Structural model

The atomic structure of icosahedral quasi-crystals may be given a description in a 6D periodic space (see Janot (1992) for an introduction). This has been shown to be the only way to retrieve structural information from experimental diffraction data (Gratias *et al* 1988, Janot *et al* 1989). In the cut scheme (Bak 1986, Janssen 1986) the periodic 6D space decomposes in two subspaces, E_{par}, the physical space, and E_{perp} the complementary space. The cubic 6D lattice is then decorated with a set of 3D objects, called atomic surfaces, which lie in the complementary space E_{perp}. Once atomic surface positions and shapes are specified, the 3D quasi-periodic structure is obtained as a cut through the decorated periodic lattice.

In the case of the i-(Al–Mn) phase, the Patterson analysis of x-ray and neutron diffraction data (Janssen 1986, Gratias *et al* 1988), together with contrast variation data (Cahn *et al* 1988), leads to a very simple model: there are three atomic surfaces located at the origin ([000000] 6D coordinates) and at the body centre (0.5[111111] 6D coordinates); Mn is located on a sphere centred on the origin and is surrounded by an Al shell, and a small Al atomic surface lies on the body centre.

2.1. *Modified Duneau–Oguey model for the Al–Mn quasi-crystal*

Taking spheres as atomic surfaces is not satisfactory, for unphysical short distances will appear in the resulting 3D quasi-periodic structure. This problem was solved by Duneau and Oguey (1989) (see also Yamamoto and Hiraga (1988)) in the ideal model that they proposed for the i-(Al–Mn) phase. (The real sample had 4–5% Si, but as a first step we consider the alloy as a binary Al–Mn alloy.) Their model is built in such a way that no short distances are generated, the atomic density and the chemical composition agree with the experimental values, and a large number of 'Mackay icosahedra' are generated in the 3D quasi-periodic structure.

Apart from atomic surfaces at the origin and at the body centre, two small atomic surfaces are located on the mid-edge of the 6D cube in their model. It has been shown that such small atomic surfaces do not show up on a Patterson map, so that this solution cannot be ruled out only on the basis of a Patterson analysis but needs a quantitative comparison with diffraction data.

The comparison of such models with experimental partial pair distribution functions showed that at least part of the atomic surfaces must be given a so-called 'parallel' component (de Boissieu *et al* 1990). In other words the location of such atomic surfaces is given by $R_{6D} + R_{par}$ where R_{6D} is either the origin, the body centre or the mid-edge of the 6D cube and R_{par} is a vector in the physical space E_{par}. A simple solution, suggested by Duneau, consists in displacing the atoms in the Mackay icosahedron. Their acceptance

domain is well defined (called *sA* in the paper by Duneau and Oguey (1989)), so that the three radii of the different shells may be free parameters. When compared with partial pair distribution functions and diffraction data, the best solution is obtained with the following parameters:

(i) small Al icosahedron: $R(A5) = 2.45$ Å;
(ii) large Mn icosahedron: $R(A5) = 4.85$ Å;
(iii) Al icosidodecahedron: $R(A2) = 4.62$ Å.

The corresponding values, when no parallel component is introduced, are 2.3 Å, 4.6 Å and 4.82 Å, respectively, i.e. the two icosahedra are expanded whereas the icosidodecahedron is retracted.

Such a modification gave a first-neighbour distance distribution close to the periodic α-(Al–Mn–Si) cubic 'approximant' periodic phase (Cooper and Robinson 1966) (see figures 1–3 later). This is particularly true for the Al–Al correlations, which have only two main components at 2.6 and 2.9 Å when no parallel component is introduced, whereas the distribution splits over five neighbours when a parallel component is introduced (see figure 3). This is the only way to achieve agreement with the measured partial pair distribution function.

2.2. The rational approximants

The calculation of the dynamical response function of the quasi-crystal can be performed using a 3D quasi-periodic cluster, obtained by a cut of the 6D model. However, such a calculation was found to be influenced by surface atoms, even for relatively large clusters. To avoid this problem, periodic boundary conditions were used.

A rational periodic approximant may be obtained easily from the 6D model. We used cubic approximants, by applying a linear phason strain to the periodic space. Practically this is done by replacing the golden mean τ by its rational approximant p/q in the phason part of the 6×6 matrix that transforms a 6D vector $\boldsymbol{R}$ into its components (R_{par}, R_{per}) in physical and perpendicular space (Elser and Henley 1985, Cahn *et al* 1988, Qiu and Jaric 1989). Atomic surfaces also need to be deformed according to the same transformation, for short distances would otherwise appear (Lançon and Billard 1990).

Some of the characteristics of the various approximants used in the calculations are given later in figures 1–3 and table 2 and are compared with the periodic α-(Al–Mn–Si) cubic crystal and with a quasi-periodic cluster.

3. Dynamical model

The choice of the interatomic potential model for an alloy such as Al–Mn is conditioned, firstly by the large proportion of Al atoms for which the interatomic interactions are known to be correctly described by central forces (Walker 1956) and, secondly, by the distribution of equilibrium interatomic distances.

In figures 1, 2 and 3 the Mn–Mn, Al–Mn and Al–Al distance histograms, respectively, are reported. In each figure, one can see from the top to the bottom the crystalline α-phase (Cooper and Robinson 1966), the 1/1 approximant, the 8/5 approximant and the quasi-crystal (the modified Duneau–Oguey model).

It can be easily seen in these figures that for all structures the distribution of interatomic distances between first neighbours is relatively broad for each type of atomic couple. In such a condition it is no longer possible to assume a simple Lennard–Jones-type potential to

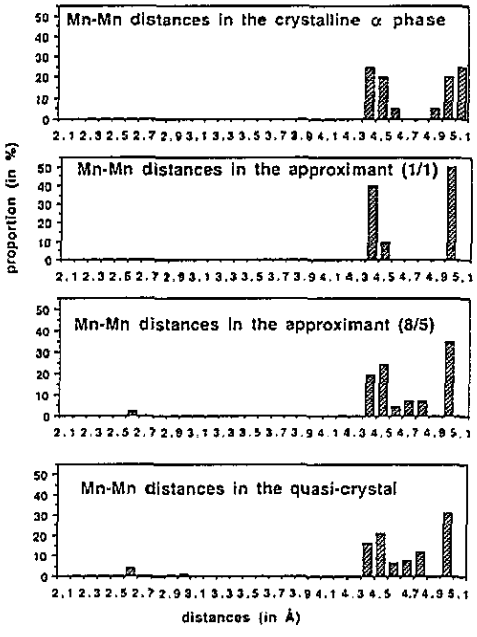

Figure 1. Mn–Mn distance histograms for Al–Mn alloys.

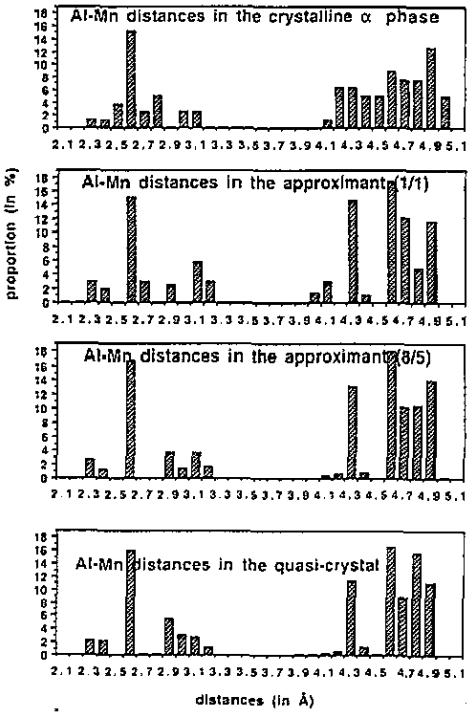

Figure 2. Al–Mn distance histograms for Al–Mn alloys.

describe the interatomic interactions in Al–Mn alloys; in fact the stability can be obtained only with relatively large relaxation displacements of the atoms which lead to an inadequate shape of the density of states (DOS) and to sound velocities lower than experimental values. Lançon and Billard (1990) using a Morse-type potential obtained a stable structure but also after significant relaxation displacements of the atoms.

3.1. Effective potential function

So, in order to calculate the dynamical properties of the i-(Al–Mn) phase in the modified Duneau–Oguey model without any atomic relaxation displacement we choose an effective local potential function of the form

$$V = \sum_{i>j} V_{ij}^{(\gamma_{ij})} \tag{3.1}$$

with

$$V_{ij}^{(\gamma_{ij})} = \tfrac{1}{2} k^{(\gamma_{ij})}(r_{ij}^{e})(r_{ij} - r_{ij}^{e})^2. \tag{3.2}$$

This form, invariant with respect to rotation and translation of the Cartesian frame, is a generalization of that developed by Walker (1956) for aluminium. In equation (3.2) the force constant $k^{(\gamma_{ij})}(r_{ij}^{e})$ depends upon the type of the i–j bond ($(\gamma_{ij}) = 1$, 2 or 3 for Mn–Mn, Mn–Al or Al–Al bonds, respectively) and is linear with the equilibrium distance r_{ij}^{e} with different behaviours for first and second neighbours, as shown in figure 4.

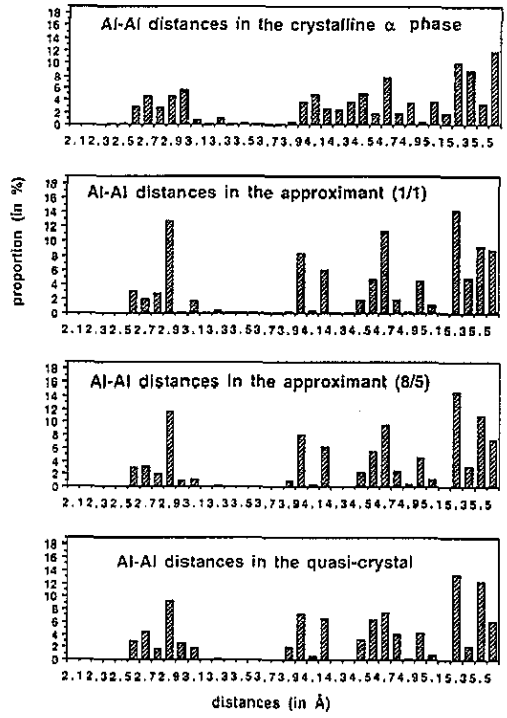

Figure 3. Al–Al distance histograms for Al–Mn alloys.

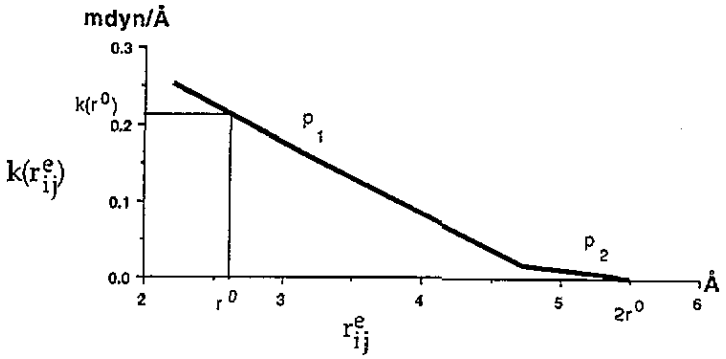

Figure 4. The variation in the effective force constants versus the equilibrium distance. The two slopes p_1 and p_2 can be reduced to dimensionless constants α and β with $\alpha = p_1 k(r^0)/r^0$ and $\beta = p_2 k(r^0)/r^0$.

For each atomic pair type the potential depends upon four constants: the mean first-neighbour equilibrium distance r^0, the force constant $k(r^0)$, the reduced slopes α and β (in r^0 and $k(r^0)$ units) of the two straight lines. In fact we have chosen the same slopes for all types of pair in order to use the minimum number of parameters.

3.2. Determination of the constants and derivation of the dynamical matrices

These constants are adjusted in the following way: we assume that the 1/1 approximant is a good approximation for the crystalline α-phase and the parameters are fitted to the sound velocities (Amazit *et al* 1992) and the one-phonon DOS curve (Miceli *et al* 1986). The distances r^0 are given by neutron diffraction studies on Al–Mn–Si alloys (Dubois *et al* 1988). In table 1 we report the complete list of adjusted Al–Mn potential constants.

Table 1. Al–Mn effective potential constants. α and β are the dimensionless reduced slopes of the two straight lines in figure 4.

Type of bond	r^0 (Å)	$k(r^0)$ (mdyn Å^{-1})	$\alpha = p_1 k(r^0)/r^0$	$\beta = p_2 k(r^0)/r^0$
Mn–Mn	2.67	0.208	−1.316	−0.187
Al–Mn	2.54	0.289	−1.316	−0.187
Al–Al	2.83	0.140	−1.316	−0.187

Using the harmonic part of this potential in Cartesian coordinates, the derivation of the dynamical matrix for any approximant, taking into account the periodic boundary conditions, is straightforward. The same calculation can be easily done also for any spherical cluster of the quasi-crystal, but it is better to calculate the dynamical properties of large approximants rather than those of quasi-crystalline clusters in order to avoid the problems due to surface modes.

Table 2 gives, for all calculated approximants, the edge of the cubic cell, the number of atoms in the cell, the chemical formulae and the number of non-zero elements in the dynamical matrix.

Table 2. The seven first approximants of the icosahedral phase of Al–Mn in the modified Duneau–Oguey model.

Approximant	Edge a of the cell (Å)	Number of atoms in a cell	Chemical formula	Number of matrix elements
1/1	12.64	122	$Al_{80.33}Mn_{19.67}$	22 142
2/1	20.46	521	$Al_{80.04}Mn_{19.96}$	91 453
3/2	33.10	2 022	$Al_{76.71}Mn_{23.29}$	330 370
5/3	53.55	8 852	$Al_{77.90}Mn_{22.10}$	1 481 568
8/5	86.65	37 381	$Al_{77.82}Mn_{22.18}$	6 254 239
13/8	140.21	158 600	$Al_{77.86}Mn_{22.14}$	26 545 186
21/13	226.86	668 236	$Al_{77.75}Mn_{22.25}$	111 157 886

4. Computational techniques

The inelastic scattering cross section of slow neutrons by condensed matter is given by the well known expression (Lovesey 1986, Benoit 1989)

$$\frac{d^2\sigma}{d\Omega\, d\omega} = \frac{k}{k_0}\hbar \sum_j |F_j(Q_d)|^2 \frac{1}{2\omega_j}[(n_j+1)\delta(\omega-\omega_j) + n_j\delta(\omega+\omega_j)] \qquad (4.1)$$

where $\omega > 0$ corresponds to neutron energy loss, and with

$$F_j(Q_d) = \sum_n b_n \frac{\exp(-W_n)}{\sqrt{m_n}} e_j(n) \cdot Q_d \exp[-iQ_d \cdot r(n)]. \tag{4.2}$$

In these expressions $e_j(n)$, m_n, b_n and $\exp(-W_n)$ are the nth atomic amplitude of the jth mode with frequency ω_j, the nth atomic mass, the Fermi scattering length and the Debye–Waller factor, respectively. $n_j = n(\omega_j) = [\exp(\beta\hbar\omega_j) - 1]^{-1}$ with $\beta = 1/kT$ is the Boltzmann factor. k_0 and k are the incident and scattered neutron wavevectors, respectively. $Q_d = k_0 - k$ is the scattering vector.

4.1. The spectral moments method (Benoit 1987, 1989, Benoit et al 1992)

One can show that (4.1) is equivalent to

$$d^2\sigma/(d\Omega\, d\omega) = (k/k_0)\hbar\{1/[1 - \exp(-\beta\hbar\omega)]\}S'(Q_d, \omega) \tag{4.3}$$

with

$$S'(Q_d, \omega) = \sum_j |F_j(Q_d)|^2 \frac{1}{2\omega_j}[\delta(\omega - \omega_j) - \delta(\omega + \omega_j)]$$

and, for $\omega > 0$, $S'(Q_d, \omega)$ can be replaced by

$$\bar{S}(Q_d, u) = \sum_j |F_j(Q_d)|^2 \delta(u - \lambda_j) \tag{4.4}$$

with $u = \omega^2$ and $\lambda = \omega_j^2$.

So the spectral moments method can be applied to determine the inelastic neutron scattering cross section. This is done in the following way: we introduce the vector $t^{(0)}$ such that

$$t^{(0)} = \sum_{n\alpha} q_n^\alpha e_n^\alpha \tag{4.5}$$

where $\alpha = x, y, z$ with

$$q_n^\alpha = b_n[\exp(-W_n)/\sqrt{m_n}]Q_d^\alpha \exp[-iQ_d \cdot r(n)]$$

in the site representation e_n^α. Then, the moments of the function $\bar{S}(Q_d, u)$ are directly derived from the dynamical matrix $\mathbf{D}$ of the sample by

$$\mu_n = \int \bar{S}(Q_d, u)u^n\, du = (t^0, \mathbf{D}^n t^0) \tag{4.6}$$

where (A, B) is the usual scalar product. In fact it is better to use generalized moments and it can be shown that

$$\bar{S}(Q_d, u) = (1/\pi) \lim_{\varepsilon \to 0_+} \{\mathrm{Im}[R(Q_d, z)]\} \tag{4.7}$$

Table 3. Effective Fermi scattering lengths and statistical weights for Al and Mn.

$b_+^{Al} = 3.669$ fm	$g_+^{Al} = \frac{7}{12}$
$b_-^{Al} = 3.141$ fm	$g_-^{Al} = \frac{5}{12}$
$b_+^{Mn} = -2.217$ fm	$g_+^{Mn} = \frac{7}{12}$
$b_-^{Mn} = -5.848$ fm	$g_-^{Mn} = \frac{5}{12}$

with

$$z = u + i\varepsilon$$

and

$$R(Q_d, z) = 1/\{z - a_1 - b_1/[z - a_2 - b_2/(z - a_3 - b_3/\ldots)]\}. \tag{4.8}$$

The coefficients of the continued fraction are given by

$$a_{n+1} = \bar{\nu}_{nn}/\nu_{nn} \qquad b_n = \nu_{nn}/\nu_{n-1\,n-1}$$

where the generalized moments are defined by

$$\nu_{nn} = (t^{(n)}, t^{(n)}) \qquad \bar{\nu}_{nn} = (t^{(n)}, \mathbf{D}t^{(n)})$$

with the recursion relation

$$t^{(n+1)} = (\mathbf{D} - a_{n+1}\mathbf{I})t^{(n)} - b_n t^{(n-1)}. \tag{4.9}$$

Knowledge of $\mathbf{D}$ and $t^{(0)}$ (all $t^{(-n)} = 0$) leads to the calculation of the a_n and b_n coefficients by a recursive procedure; so it is possible to derive the inelastic neutron scattering cross section without any diagonalization.

4.2. Introduction of the incoherent part of the cross section

It is important to remark that working with very large samples the spectral moments method allows us to take into account the isotopic disorder of the system. So the calculated differential cross section can be compared directly with the experimental results. In particular, it is possible to introduce into the cross section formulae (4.1) and (4.2) all the scattering features relative to any given atom. The 'disorder' due to isotope distribution and/or the existence of nuclear spins leads to the so-called incoherent part of the neutron scattering cross section. This can easily be done by the introduction for each atom individually of an effective Fermi scattering length $b_\pm^{is}$ which depends not only on the chemical nature of the atom but also on the isotope considered and on the coupling of the nuclear spin I with the neutron spin:

$$b_+^{is} = b_c^{is} + \sqrt{I/(I+1)}\,b_i^{is} \tag{4.10}$$

with a statistical weight $g_+ = (I+1)/(2I+1)$, and

$$b_-^{is} = b_c^{is} - \sqrt{(I+1)/I}\,b_i^{is} \tag{4.11}$$

with a statistical weight $g_- = I/(2I+1)$, where b_c^{is} and b_i^{is} are the coherent and incoherent Fermi scattering lengths for the isotope is.

In the cross section calculation (4.1) and (4.2) the scattering lengths $b_\pm^{is}$ are affected by the atoms according to a random distribution taking into account the statistical weights $g_\pm$ and the isotope proportions in the natural atomic species under consideration.

In the case of Al–Mn alloys there is no isotope distribution; only nuclear spins need to be considered. Al and Mn have a $\frac{5}{2}$ nuclear spin; so from published tables (Sears 1984) we deduce the values of $b_\pm^{is}$ given in table 3. These values have been used in all subsequent calculations.

4.3. Derivation of the weighted one-phonon DOS

When the inelastic neutron scattering spectra are recorded on powder samples, the experimental results lead, after some transformations, to a neutron-weighted vibrational DOS for the studied sample (Lustig *et al* 1985, Suck *et al* 1980). In order to make a comparison with these experiments we have calculated the same quantities using an improvement of the spectral moments method (Benoit *et al* 1992).

The neutron-weighted vibrational DOS obtained after averaging is given by (Lustig *et al* 1985, Suck *et al* 1980)

$$\bar{g}(E) = \left[\left(\frac{\bar{\sigma}}{m}\right)\right]^{-1} \exp(2\bar{W}) \sum_{\alpha} \frac{C_\alpha \sigma_\alpha}{m_\alpha} \langle (\hat{Q} \cdot e_\alpha)_E^2 \exp(-2W_\alpha) \rangle g_\alpha(E) \quad (4.12)$$

which can be written

$$\bar{g}(E) = \left[\left(\frac{\bar{\sigma}}{m}\right)\right]^{-1} \sum_{\alpha} \frac{C_\alpha \sigma_\alpha}{m_\alpha} g_\alpha(E) \quad (4.13)$$

if we neglect the polarization and Debye–Waller factors. $g_\alpha(E)$ is the partial vibrational DOS, C_α the concentration, σ_α the coherent scattering cross section and m_α the mass of α species atoms. $g_\alpha(E)$ is defined as the sum of the local DOS over all atoms of the α species.

$\bar{g}(E)$ can be easily calculated in the following way: we consider working vectors $t^{(0)}(\alpha)$ for each atom species. The components of these vectors are random variables according to the method described by Benoit *et al* (1992). Then they are normalized according to the factors included in equation (4.13). It is also possible in this case to take into account the incoherence due to isotopes and spin disorder as explained in section 4.2.

All computations have been performed on an IBM 3090-600 VF. As shown in table 2 the rank of the matrix for the 21/13 approximant is higher than 2 000 000 with more than 110 000 000 non-zero elements. Special matrix storage techniques have been developed for this work.

5. Results

The dynamical properties of crystalline and quasi-crystalline phases of Al–Mn have been calculated through the rational approximants of the modified Duneau–Oguey (1989) model (de Boissieu *et al* 1990): 1/1 for the α crystalline phase, and 2/1, 3/2, 5/3, 8/5, 13/8 and 21/13 for the icosahedral phase.

However, as can be seen in the results, there is very little difference between the highest two approximants: 13/8 and 21/13. So we believe that the 13/8 approximant is a good model to represent the true infinite quasi-crystal.

5.1. The weighted DOS for the crystal and quasi-crystal

Theoretical neutron-weighted DOSs for the 1/1, 8/5 and 13/8 approximants are reported in figure 5. They can be compared with the experimental results (reported in figure 6) obtained by Miceli *et al* (1986) with crystalline and quasi-crystalline $Al_{0.8}Mn_{0.2}$ alloy powders.

We note that the agreement is good for the crystalline phase. For the icosahedral phase a DOS reduction appears at the centre of the frequency spectrum. This feature increases as the size of the approximant increases and is certainly due to an increase in the dispersion of the atomic environment in quasi-crystals.

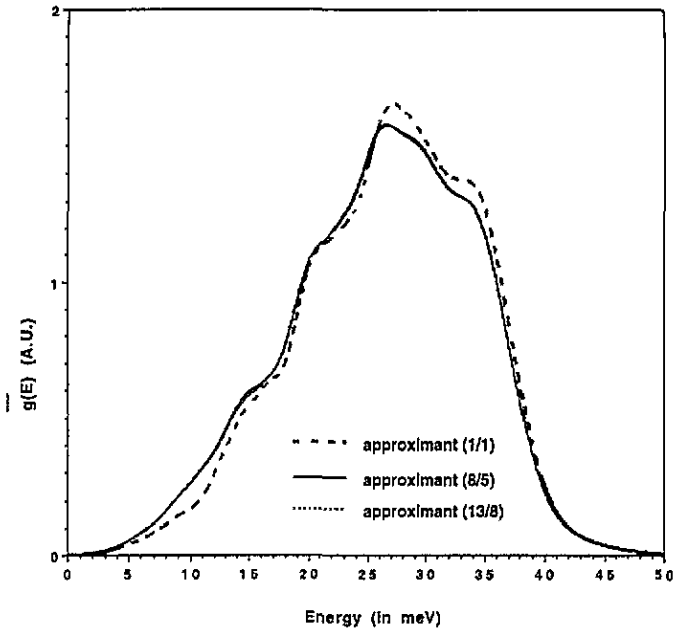

Figure 5. Calculated weighted DOS for Al–Mn alloy: rational 1/1, 8/5 and 13/8 approximants of the icosahedral phase (A.U., arbitrary units).

The DOSs of the 8/5 and 13/8 approximants are very similar; so they surely yield a good estimate for the DOS of the perfect infinite quasi-crystal. Comparison with experiment shows that the theoretical curve is a little higher than the experimental curve. The origin of this discrepancy is not clear and this point needs further investigation.

In the low-frequency region the theoretical curve for the icosahedral phase is above the curve for the crystalline phase. Such a feature has been found experimentally by Suck (1988) for Al–Mn–Si alloys.

5.2. *Inelastic neutron scattering*

The dynamical properties of the i-(Al–Mn–Pd) phase have been recently investigated through inelastic neutron scattering studies. As we saw in the introduction of this paper, these dynamical properties should be similar in both phases (i-(Al–Mn) and i-(Al–Mn–Pd)).

In order to establish a parallel between the experiments performed on a perfect Al–Mn–Pd quasi-crystal (de Boissieu *et al* 1993a, b) and the calculations on the Al–Mn model, we have investigated the inelastic neutron scattering of Al–Mn for two directions of the (Q_x, Q_y) plane of the reciprocal space.

The neutron diffraction pattern of the Al–Mn phase and the Al–Mn–Pd phase in the twofold (Q_x, Q_y) plane of the reciprocal space are shown in figure 7. The computations have been performed for some of the reciprocal space points as reported in the experimental work.

5.2.1. Pseudo-dispersion curves. We present in figure 8(a) the results of the computation of the inelastic scattering cross sections between the points D and E of the (Q_x, Q_y) plane and in figure 8(b) the already-published results on Al–Mn–Pd for the same points.

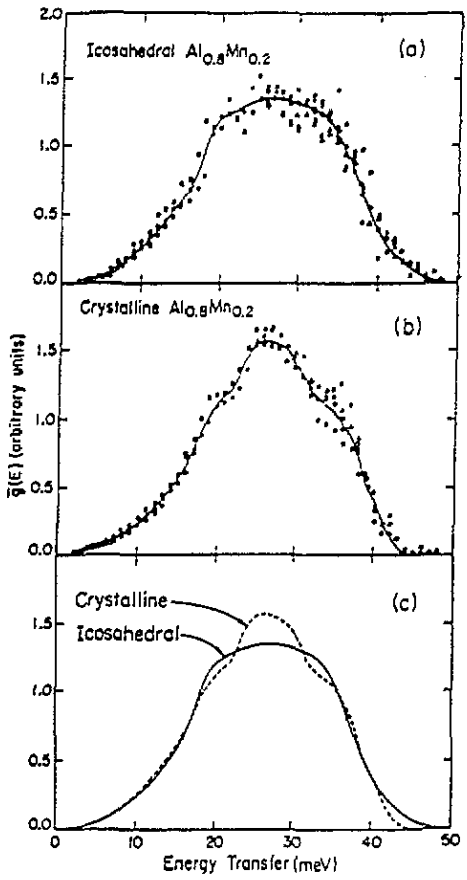

Figure 6. Experimental weighted DOSS for $Al_{0.8}Mn_{0.2}$ (from Miceli *et al* 1986): (*a*) icosahedral phase; (*b*) α crystalline phase; (c) comparison.

In both spectra we can follow a transverse acoustic mode (indicated by an arrow) originating from the Bragg peak D. The acoustic phonon branch originating from the Bragg peak E is not as clearly defined. These peaks (indicated by crosses) are more intense in the Al–Mn modelization than in Al–Mn–Pd. Finally, from D to E, we can follow a shoulder (indicated by an asterisk) on the high-frequency side of the acoustic peak originating from D. This shoulder corresponds to the longitudinal acoustic branch originating from C. The experimental and calculated pseudo-dispersion curves are reported in figure 9.

Previous results obtained by calculation on 1D systems (Ashraff and Stinchcombe 1989, Benoit *et al* 1990, Azougarh 1991), i.e. the existence of pseudo-dispersion curves and quasi-Brillouin zones in quasi-crystalline structures are now well established experimentally for Al–Fe–Cu alloy (Quilichini *et al* 1990, 1992, 1993), Al–Li–Cu alloy (Goldman *et al* 1991, 1992) and Al–Mn–Pd alloy (de Boissieu *et al* 1993a, b). They are here confirmed by a physically realistic 3D model.

If the presence of Pd does not change the acoustic modes greatly (apart from a scaling factor), the frequencies of the optic modes are strongly shifted, as can be expected from the comparison of the experimental weighted DOSS for Al–Mn (Miceli *et al* 1986) and Al–Mn–Pd (Suck 1993). This explains the presence of the 5 THz peak found for Al–Mn and completely absent for Al–Mn–Pd (figure 8).

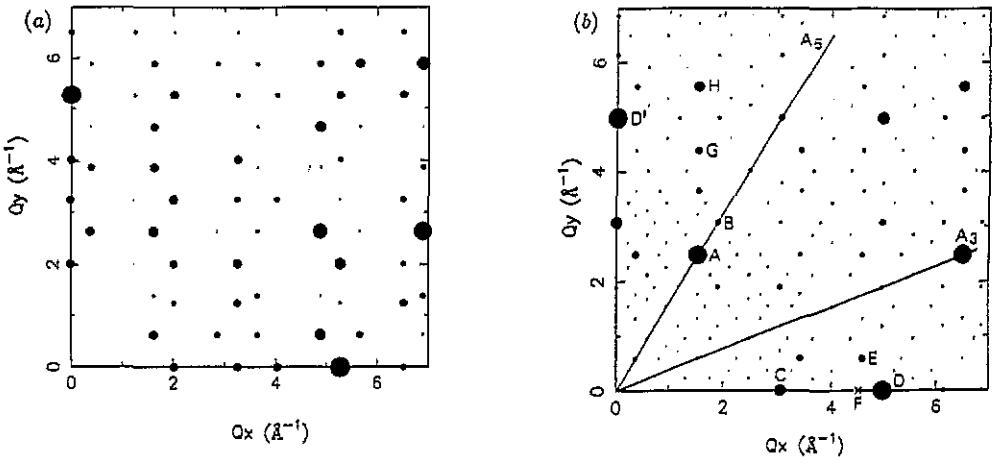

Figure 7. Twofold (Q_x, Q_y) reciprocal scattering plane of (*a*) the i-(Al–Mn) and (*b*) the i-(Al–Mn–Pd) phases. The area of the spots is proportional to the intensity of the corresponding Bragg peaks.

5.2.2. Broadening. We reproduce, in figure 10(*a*), 12 experimental constant-Q_d spectra (de Boissieu *et al* 1993a) for Al–Mn–Pd. The corresponding momentum transfers Q_d are of the form $Q_d = Q_B + q$ where Q_B refers to the Bragg spot D in figure 7 and q is directed along Q_y. We present the results of the computation, for the 1/1 approximant in figure 10(*b*) and for the 13/8 approximant in figure 10(*c*) of Al–Mn, for the first six spectra. Finally we report in figure 10(*d*) the behaviour of the inelastic neutron scattering cross section computed at point D1, ($|q| = 0.45$ Å^{-1}), for all approximants from 1/1 to 21/13.

We note that, as in the experiment, the width (after deconvolution) of the acoustic phonon line increases as the phonon wavevector (or the frequency) increases. These effects have been already mentioned by Quilichini *et al* (1992, 1993) for Al–Fe–Cu.

We report in figure 11 the behaviour of the five first peak widths (after deconvolution) as a function of the size of the approximants. For the 1/1 and 2/1 approximants the width corresponds to the phonon lifetime introduced in the computation (ε in equation (4.7)); so the deconvoluted width is in fact zero and no special effects are observed. The broadening becomes noticeable from the 3/2 approximant upwards and is nearly the same for the highest approximants.

The change in width with phonon wavevector agrees very well with the experimental observation if we use at least the fourth approximant. To show this feature we have reproduced in figure 12 the Al–Mn–Pd experimental deconvoluted width curve (de Boissieu *et al* 1993a) and the corresponding curve obtained with the highest approximants of the i-(Al–Mn) phase.

Figure 10(d) is a good illustration of the effect of approximant size on the line position and lineshape. We note that, for a given phonon vector, the peak frequency strongly depends on the approximant size. It is necessary to work with at least the fourth approximant to obtain stabilization of the frequency at the quasi-crystal value.

6. Discussion

We focus our attention on the broadening of the acoustic phonon lines. It is interesting to

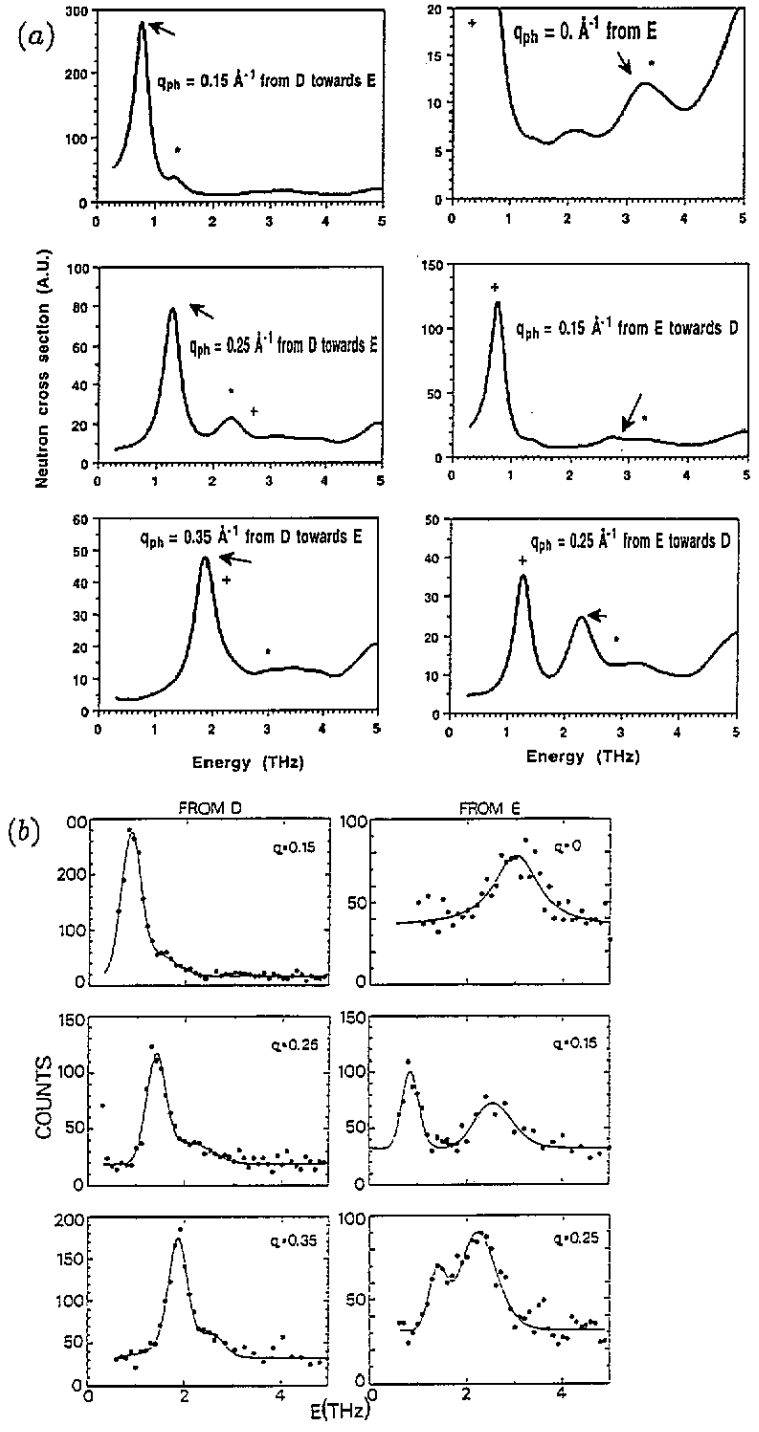

Figure 8. (*a*) Computed inelastic scattering cross sections for points between D and E for Al–Mn higher approximants (A.U., arbitrary units): ↑, transverse acoustic peaks from D; +, transverse acoustic peaks from E; ∗, longitudinal acoustic peaks from D. q_{ph} stands for $|q|$. (*b*) Experimental inelastic scattering cross sections of an Al–Mn–Pd quasi-crystal for points between D and E (from de Boissieu *et al* 1993a).

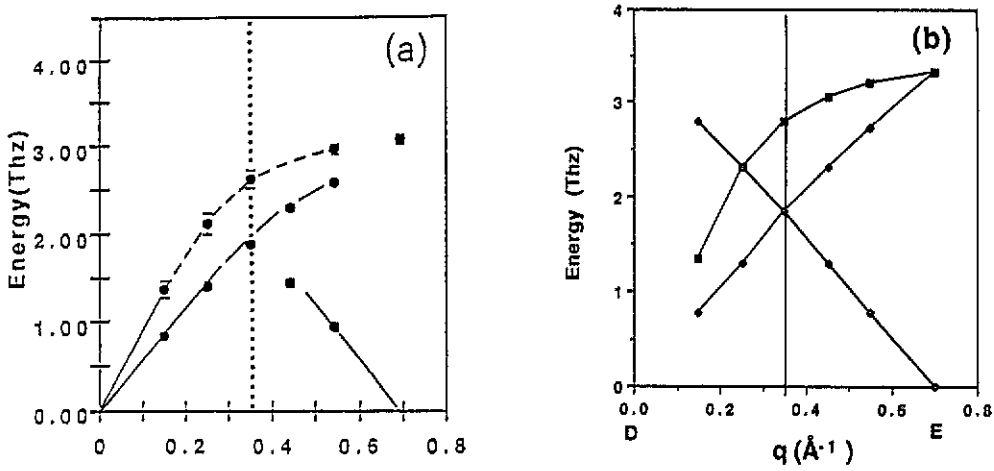

Figure 9. Experimental and calculated dispersion curves between the points D and E. (*a*) Experimental curves from de Boissieu *et al* (1993b). (*b*) Calculated curves: □, transverse acoustic peaks from D; ↑, transverse acoustic peaks from E; ■, longitudinal acoustic peaks from D.

compare the quasi-crystal on the one hand with perfect crystalline systems and on the other hand with metallic amorphous systems.

For perfect crystalline systems, if the anharmonicity is not too strong, the linewidth is a constant. This is related to the infinite spatial extension of the modes.

For metallic amorphous systems it has been shown by Hafner (1981, 1983a, b, 1985) that it is possible to define one, and only one, Brillouin zone. The neutron scattering spectra exhibit sharp inelastic peaks near $Q_d = 0$ and it is also possible to obtain the longitudinal acoustic dispersion curve. The inelastic peaks exhibit a large broadening with increasing momentum transfer. This broadening is a consequence of the localized character of the vibrational modes in amorphous systems. Figure 13 taken from the work of Leadbetter (1973) illustrates these features nicely.

For a quasi-crystal with long-range order it is possible to observe acoustic modes associated with strong Bragg spots. In the 1D model (Fibonacci chain) it has been shown (Benoit *et al* 1990) that there are several *continua* of critical modes and that localization increases with increasing frequency. In the 3D model, from equation (4.2), we note that, for systems with only one atom species, the inelastic scattering cross section is directly related to the spatial Fourier transform of the mode eigenvectors. So it is natural to interpret the increasing width of acoustic peaks with increasing frequency as a consequence of the increasing degree of localization. However, owing to the long-range order character of the quasi-crystalline structure, the localization is certainly 'critical', as there is no reason for localization in a particular region of the structure.

Results obtained by Los *et al* (1993) are derived from a 3D icosahedral Penrose tiling model. They studied the scaling behaviour of the spectrum by a multifractal analysis. Their main results concern the existence of localized modes only in the very upper end of the spectrum, the other states being normal extended states. They conclude that the phonon states behave more critically in the Fibonacci chain than in the icosahedral Penrose tiling. Our 3D model, which is realistic since it simulates the properties of the Al–Mn quasi-crystal, leads to slightly different conclusions concerning the character of the eigenmodes; in our calculations the localized character appears progressively with increasing frequency.

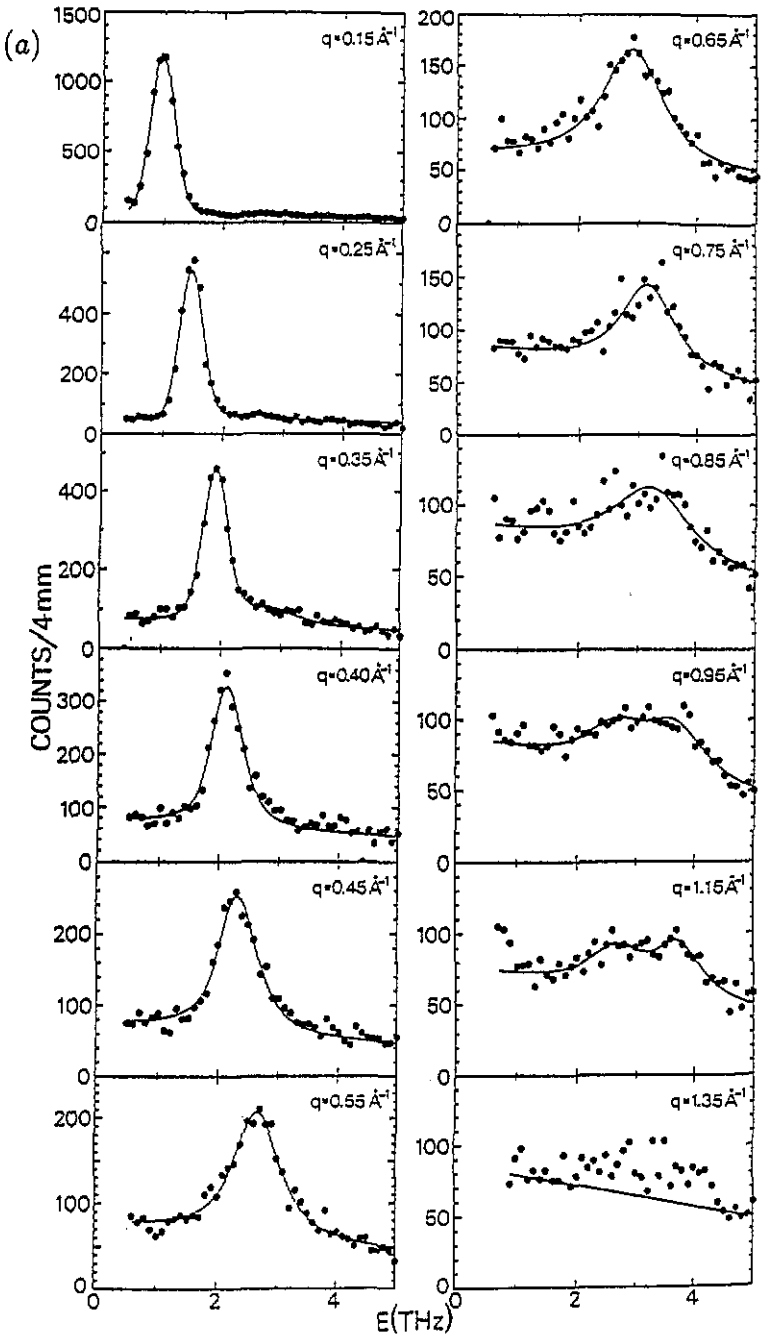

Figure 10. (*a*) Experimental inelastic scattering cross sections of an Al–Mn–Pd quasi-crystal for 12 points from Bragg spot D in the Q_y direction (from de Boissieu *et al* 1993a). (*b*) Computed inelastic scattering cross sections for six points from Bragg spot D in the Q_y direction for the Al–Mn 1/1 approximant (A.U., arbitrary units). The six curves from the left to the right correspond to $q = 0.15$ Å^{-1}, 0.25 Å^{-1}, 0.35 Å^{-1}, 0.40 Å^{-1}, 0.45 Å^{-1} and 0.55 Å^{-1}, respectively. (*c*) Computed inelastic scattering cross sections for six points from Bragg spot D in the Q_y direction for the Al–Mn 13/8 approximant (nearly quasi-crystalline phase) (A.U., arbitrary units). The six curves from the left to the right correspond to $q = 0.15$ Å^{-1}, 0.25 Å^{-1}, 0.35 Å^{-1}, 0.40 Å^{-1}, 0.45 Å^{-1} and 0.55 Å^{-1}, respectively. (*d*) Calculated transverse inelastic neutron scattering for $q = 0.45$ Å^{-1} for the first seven rational approximants (A.U., arbitrary units).

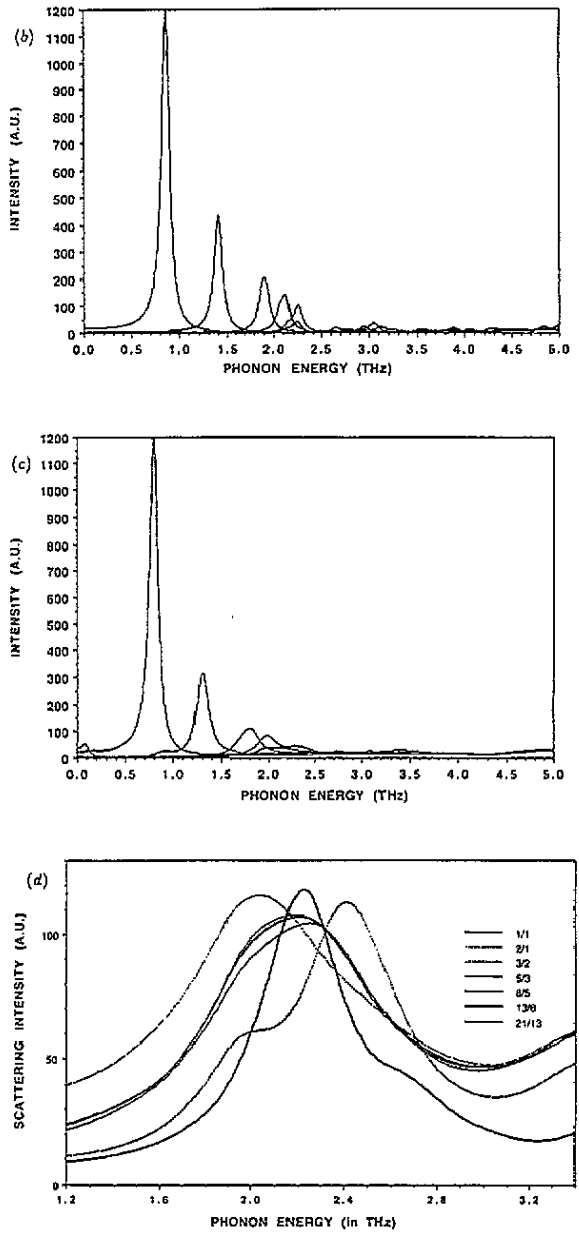

Figure 10. (Continued)

Recent work by Hafner and Krajči' (1993) confirms the existence of localized modes (they used the expression 'confined' modes) due to local topological frustrations, in a 3D model for i-(Al–Zn–Mg). They used, for the calculation of the scattering cross section, either diagonalization or the recursion method (until the 5/3 approximant with 12 380 atoms for i-(Al–Zn–Mg)). Our calculation method (the spectral moments method) allows us to calculate the inelastic neutron scattering cross section, and the DOS for larger approximants (until the 21/13 approximant with 668 236 atoms for i-(Al–Mn)), taking into account isotopic and

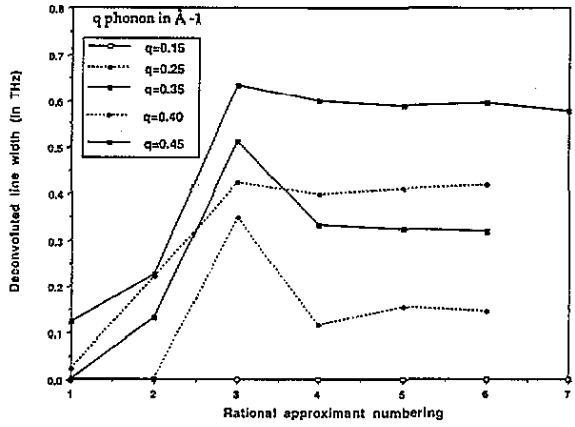

Figure 11. Calculated widths of inelastic neutron scattering peaks for rational approximants of an Al–Mn quasi-crystal.

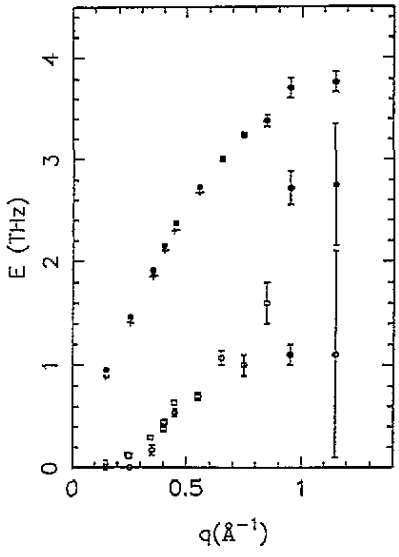

Figure 12. Experimental and calculated dispersion and deconvoluted width curves for points from Bragg spot D in the Q_y direction: ○, experimental widths; □, calculated widths; ●, the experimental peak energies; +, calculated peak energies.

incoherent effects.

To illustrate the relation between localization and width we develop a 1D model where the eigenvectors are a convolution product between a localized mode and a 'Dirac comb':

$$e_j(n) = \sum_{n'N} \phi_j(r_n - r_{n'})\delta(r_{n'} - R_N) \tag{6.1}$$

where the r_n are the equilibrium positions of the particles ($r_n = na$), the R_N the positions of the Dirac peaks and the $\phi_j(u_n)$ the localized wavefunctions. Taking

$$\phi_j(u_n) = \exp(-\gamma_j|u_n|)\exp(ik_j u_n) \tag{6.2}$$

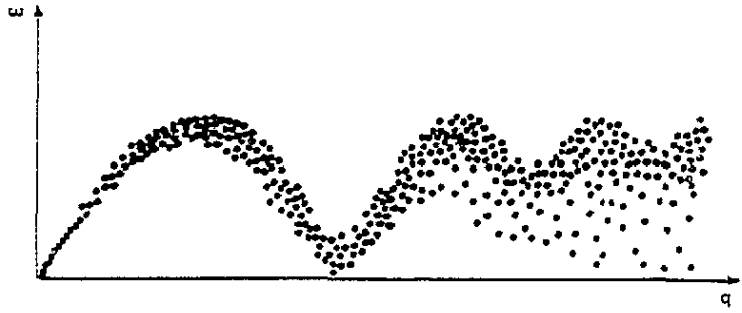

Figure 13. Phonon dispersion in an amorphous system (taken from Leadbetter 1973).

with

$$\gamma_j = \omega_j/g \qquad k_j = \omega_j/v \tag{6.3}$$

(Debye model) v being the sound velocity, k_j the phonon wavevector and $1/\gamma_j$ the localization factor, it is easy to show that the neutron cross section given by (4.1) behaves as

$$\sigma(\omega, Q_d) \simeq \left[\!\left[\frac{\{1 - \exp[-2(\omega/g)a]\}}{\{1 + \exp[-2(\omega/g)a] - 2\exp[-(\omega/g)a]\cos[(\omega/v - Q_d)a]\}} \right]\!\right]^2 \tag{6.4}$$

apart from a form factor depending on the particular structure of the Dirac comb. This expression is obtained by changing the discrete summation over j in (4.1) by a continuous summation over the frequency ω.

The results of equation (6.4) are shown in figure 14 where six inelastic neutron scattering spectra are plotted. The six spectra correspond to $Q_d = Q_B + rq_0$, $r = 1, 2, 3, \ldots$ (with q_0 arbitrary fixed and $Q_B = 0$). It can be easily seen in figure 14 that the broadening of the line is proportional to ω (or to $q = rq_0$), as it can be deduced from a limited expansion of equation (6.4). So the critical character of the modes induces a broadening of the acoustic phonon peaks, the intensity of these peaks depending on the form factor of the Dirac comb.

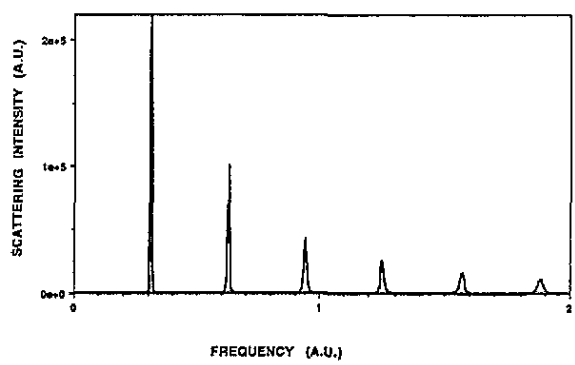

Figure 14. 1D inelastic neutron scattering cross sections for a chain with 'critical' modes (A.U., arbitrary units). The six spectra from left to right correspond to $Q_d = Q_B + q$, with $Q_B = 0$ and $q = q_0, 2q_0, 3q_0, \ldots$ with q_0 arbitrarily fixed.

As a conclusion, in quasi-crystals, the long-range order gives rise to acoustic sheets near the intense Bragg spots. This effect has already been mentioned for 1D systems and is now well established experimentally and theoretically for 3D systems. The behaviour of the phonon peak widths can be easily interpreted as due to the existence of *continua* of 'critical' modes. These modes become more and more 'critical' as the peak frequency increases.

To confirm the 'critical' character of the modes in a 3D realistic quasi-crystalline system, further investigation will be necessary especially by the Green function technique.

Acknowledgments

Fruitful discussions with C Janot and T Janssen are acknowledged. This work was supported by IBM France and the Centre National Universitaire Sud de Calcul (Ministère de l'Education Nationale), contract C3NI (High Performance Computing).

References

Amazit Y, de Boissieu M and Zarembowitch A 1992 *Europhys. Lett.* **20** 703
Ashraff J A and Stinchcombe R B 1989 *Phys. Rev.* B **39** 2670
Azougarh A 1991 *Thèse* Montpellier
Bak P 1986 *Scr. Metall.* **20** 1199
Benoit C 1987 *J. Phys. C: Solid State Phys.* **20** 765
—— 1989 *J. Phys.: Condens. Matter* **1** 335
Benoit C, Poussigue G and Azougarh A 1990 *J. Phys.: Condens. Matter* **2** 2519
Benoit C, Royer E and Poussigue G 1992 *J. Phys.: Condens. Matter* **4** 3125
Cahn J W, Gratias D and Mozer B 1988 *J. Physique* **49** 1225
Cooper M and Robinson K 1966 *Acta Crystallogr.* **20** 614
de Boissieu M, Boudard M, Bellissent R, Quilichini M, Hennion B, Currat R, Goldman A I and Janot C 1993a *J. Phys.: Condens. Matter* **5** 4943
de Boissieu M, Boudard M, Moudden H, Quilichini M, Bellissent R, Hennion B, Currat R, Goldman A I and Janot C 1993b *Proc. 4th Int. Conf. on Quasicrystals (St Louis, MO, 1992) J. Non-Cryst. Solids* **153–4** 552
de Boissieu M, Janot C and Dubois J-M 1990 *J. Phys.: Condens. Matter* **2** 2499
Dubois J M, Janot C and de Boissieu M 1988 *Quasicrystalline Materials* ed C Janot and J M Dubois (Singapore: World Scientific) p 97
Duneau M and Oguey C 1989 *J. Physique* **50** 135
Elser V and Henley C L 1985 *Phys. Rev. Lett.* **55** 2883
Goldman A I, Stassis C, Bellissent R, Moudden H, Pyka N and Gayle F W 1991 *Phys. Rev.* B **43** 8763
Goldman A I, Stassic C, de Boissieu M, Currat R, Janot C, Bellissent R, Moudden H and Gayle F W 1992 *Phys. Rev.* B **45** 10 280
Gratias D, Cahn J W and Mozer B 1988 *Phys. Rev.* B **38** 1643
Hafner J 1981 *J. Phys. C: Solid State Phys.* **14** L287
—— 1983a *Phys. Rev.* B **27** 678
—— 1983b *J. Phys. C: Solid State Phys.* **16** 5773
—— 1985 *J. Non-Cryst. Solids* **75** 253
Hafner J and Krajči' M 1993 *J. Phys.: Condens. Matter* **5** 2489
Janot C 1992 *Quasicrystal: A Primer* (Oxford: Oxford University Press)
Janot C, de Boissieu M, Dubois J M and Pannetier J 1989 *J. Phys.: Condens. Matter* **1** 1029
Janssen T 1986 *Acta Crystallogr.* A **42** 261
—— 1988 *Quasicrystalline Materials* ed C Janot and J M Dubois (Singapore: World Scientific) p 327
Lançon F and Billard L 1990 *J. Physique* **51** 1099
Leadbetter A J 1973 *Chemical Applications of Thermal Neutrons Scattering* ed B T M Willis (Oxford: Oxford University Press) p 146
Los J 1993 *Thesis* Nijmegen
Los J, Janssen T and Gähler F 1993 *J. Physique* **3** 107

Lovesey S W 1986 *Theory of Neutron Scattering from Condensed Matter* vol 1 (Oxford: Oxford University Press)
Lustig N, Lannin J S, Carpenter J M and Hasegawa R 1985 *Phys. Rev.* B **32** 2778
Miceli P F, Youngquist S E, Neumann D A, Zabel H, Rush J J and Rowe J M 1986 *Phys. Rev.* B **34** 8977
Qiu S Y and Jaric M V 1989 *Proc. Anniversary Adriatic Research Conf. on Quasicrystals (Trieste 1989)* ed M V Jaric and S Lundquist (Singapore: World Scientific) p 19
Quilichini M, Heger G, Hennion B, Lefebvre S and Quivy A 1990 *J. Physique* **51** 1785
Quilichini M, Hennion B and Heger G 1993 *J. Non-Cryst. Solids* **153–4** 568
Quilichini M, Hennion B, Heger G, Lefebvre S and Quivy A 1992 *J. Physique* II **2** 125
Sears V F 1984 *Thermal Neutron Scattering Lengths and Cross Sections for Condensed Matter Research* (Chalk River, Ont.: Atomic Energy of Canada Limited)
Suck J B 1988 *Quasicrystalline Materials* ed C Janot and J M Dubois (Singapore: World Scientific) p 337
—— 1993 *J. Non-Cryst. Solids* **153–4** 573
Suck J B, Rodin H, Güntherod T, Beck H, Daubert J and Gläser V 1980 *J. Phys. C: Solid State Phys.* **13** L167
Walker C B 1956 *Phys. Rev.* **103** 547
Yamamoto A and Hiraga K 1988 *Phys. Rev.* B **37** 6207